



Contents lists available at ScienceDirect

Spectrochimica Acta Part A: Molecular and Biomolecular Spectroscopy

journal homepage: www.elsevier.com/locate/saa

Spatially-resolved mineral identification and depth profiling on chondrules from the primitive chondrite Elephant Moraine 14017 with confocal Raman spectroscopy

Sun Young Park, Changkun Park *

Division of Polar Earth-System Sciences, Korea Polar Research Institute, Incheon 21990, Republic of Korea

ARTICLE INFO

Article history:

Received 8 June 2018

Received in revised form 28 August 2018

Accepted 30 August 2018

Available online 31 August 2018

Keywords:

Confocal Raman spectroscopy

Mineral identification

Depth profiling

Primitive chondrite

ABSTRACT

Confocal Raman spectroscopy is effective in unveiling structures of minerals without destruction from surface to certain depth. In this study, we introduce an application of confocal Raman spectroscopy on minerals in a primitive chondritic meteorite. The experimental lateral resolution on silicate minerals in this study is $\sim 1.0 \mu\text{m}$. Raman spectrum of mesostasis in a named “Tear Drop” chondrule, a spherule object from a primitive chondrite, of Elephant Moraine 14017 (EET 14017) shows a broad feature indicating amorphous phase, which is a common characteristic of primitive chondrule mesostasis. Weak intensities of 825 and 858 cm^{-1} peaks were observed in the glassy mesostasis, probably originated from olivine below the surface. A plagioclase-rich chondrule (PRC-1) of EET 14017 was investigated with Raman spectroscopy, which contains two different occurrences of plagioclase: lath-shaped and interstitial grains. The strong intensity of 488 and 505 cm^{-1} (plagioclase) and weak intensity of 461 cm^{-1} band were observed on the lath-shaped plagioclase. The weak 461 cm^{-1} peak from the plagioclase is probably from the subsurface quartz. Raman spectrum of interstitial plagioclase in PRC-1 shows 488 and 505 cm^{-1} bands and weak pyroxene bands. Depth profiling conducted on the interstitial plagioclase clearly shows that pyroxene exists below the surface. High-lateral resolution and well-resolved depth profiling with the confocal Raman spectroscopy allows us to identify tiny grains and investigate hidden phases underneath the surface without destruction of extraterrestrial materials.

© 2018 Elsevier B.V. All rights reserved.

1. Introduction

Raman spectroscopy is based on a Raman scattering phenomenon. When a laser with a specific wavelength is injected into a sample, a frequency of photon changes to be higher or lower than that of initially incident laser, this is called a Raman Effect [1]. Raman spectroscopy provides information of vibrational and rotational energy of molecular bonding using Raman Effect. In Raman spectroscopy, however, some scattered light could result in peaks from surrounding phases when focus is out or the targeted phases are small and close to each other. It is often observed that spectral signatures from surrounding and/or subsurface minerals are mixed into the spectra of the primary target when analyzing terrestrial and extraterrestrial rocks with an out-of-focus laser. Confocal Raman spectroscopy is effective to observe phase change with depth and to analyze a small grain in a rock sample by removing out-of-focus signals using a pinhole aperture. Intensity of a component-specific band with the distance from sample surface to depth is obtained by change of laser focus, which provides information on structural changes as a depth profile. Spatial resolution of confocal

Raman spectroscopy in x, y, and z directions is better than that of conventional Raman spectroscopy because signals from neighboring phases are easily removed. When surrounding and/or subsurface minerals generate fluorescence with the interaction with the incident laser, these fluorescent photons cannot pass through the pinhole aperture. Thus the signal only from the focused area is detected by the confocal Raman spectrometer.

Raman spectroscopy has been used extensively in all areas of geology [2], including identification of minerals in meteorites [3–8], their classification [9,10], and shock effects on their parent bodies [11,12]. The most advantage of Raman spectroscopy is to non-destructively identify mineral polymorphs. For instance, it is difficult to distinguish SiO_2 polymorph by back-scattered electron (BSE) imaging, energy dispersive spectroscopy (EDS), and wavelength dispersive spectroscopy (WDS) using an electron microprobe. But with Raman spectroscopy, it is quick and easy to identify and separate quartz, cristobalite, tridymite, and stishovite because their Raman spectra are remarkably different [13]. Raman is also a powerful technique to probe glass and crystalline structure of minerals [4,14]. Previous Raman and infrared spectroscopic studies for olivine in terrestrial and extraterrestrial rocks showed that peak positions of olivine increase with increasing forsterite content [$\text{MgO}/(\text{MgO} + \text{FeO})$], and thus one can estimate the composition of

* Corresponding author.

E-mail address: changkun@kopri.re.kr (C. Park).

olivine (forsterite content) using Raman spectroscopy [15] and IR spectroscopy [16]. Confocal Raman spectroscopy has been widely used to study fluid inclusions in terrestrial rocks by removing signal from surrounding matrix [17–19].

Extraterrestrial rock samples, especially for chondrites, have been studied with Raman spectroscopy providing structural information on mineral components [e.g., 20,21,22]. Chondrites are specific type of cosmic sedimentary rocks formed in the early Solar System, including spherical objects (so called chondrules), metal, fine-grained matrix, and refractory inclusions [23]. Chondrites have experienced various degrees of aqueous alteration and thermal metamorphism on the parent bodies [24,25]. Based on petrographic observations and mineral chemistry, chondrites are divided into petrologic types 1 to 6. The degree of thermal metamorphism increases from type 3 to type 6, that of aqueous alteration increases from type 3 to type 1 [26]. Raman spectroscopy can be used to determine the lowest petrologic type (type 3.0–3.9) of chondrites, by using the ratio of peak intensity between D (disordered) and G (graphitic) bands and the full-width at half-maximum (FWHM) of D band of organic materials in matrices of chondrites because those are sensitive to thermal metamorphism [10,27,28].

Chondrules of primitive chondrites (type 3) generally consist of olivine and pyroxene grains and glassy mesostasis, formed by rapid cooling of chondrule melts [29]. Thermal metamorphism on the parent bodies could have resulted in recrystallization of secondary plagioclase from mesostasis. Primary plagioclase has been occasionally observed in type 3 ordinary [30–33] and carbonaceous chondrites [34–37]. Experimental studies showed that plagioclase crystallizes directly from melts of chondrule compositions at slow cooling rates $< \sim 1$ °C/h [38]. Because compositions of plagioclase and glassy mesostasis are similar, it is necessary to identify their structural differences using spectroscopic analysis. Probing the presence of primary plagioclase in chondrules is important to reveal the crystallization processes of chondrules in primitive chondrites. In this study, we explore phases of chondrule components whether they are crystalline or amorphous using a confocal Raman spectroscopy. We also provide well-resolved Raman spectra of micrometer-sized minerals, and introduce identification of minerals underneath surface in an ordinary chondrite found in Antarctica.

2. Experimental Method

2.1. Sample Description

Elephant Moraine 14017 (EET 14017) is an ordinary chondrite weighed 11.8 g, found in the Elephant Moraine, West Antarctica, by Korea expedition for Antarctic meteorites (KOREAMET) in 2014–15 season. A small chip from the meteorite was mounted in a 1-in. disk using epoxy. A thin section from the mount was polished with diamond lapping films (12, 9, 3, and 1 μm grit size), followed by diamond suspension (0.2 μm particle size) for the combined study with electron microprobe and Raman spectroscopy. Stereomicroscopic image of the section of EET 14017 shows very well defined chondrules from dark matrix (Fig. 1). The abundance of chondrule is ~ 73 vol%, a matrix content is ~ 26 vol%, and metal is rare (< 1 vol%). Based on the relatively large chondrule size (from ~ 0.4 to ~ 2.6 mm with an average of ~ 0.9 mm), rare metal, and glassy mesostasis of chondrules, the EET 14017 is classified as an LL-group ordinary chondrite and petrologic type 3.

2.2. Electron Microprobe Analysis

The polished thin section of EET 14017 was coated with approximately 25 nm thick carbon film for electron microprobe analysis. Mineral chemistry was studied with a field emission electron probe microanalyzer (FE-EPMA; JEOL JXA-8530F) at Korea Polar Research Institute (KOPRI) using a 15 keV accelerating voltage, 20 nA beam current, beam size of ~ 1 μm , with five wavelength dispersive X-ray spectrometers (WDS). Qualitative analysis with an energy dispersive spectrometer

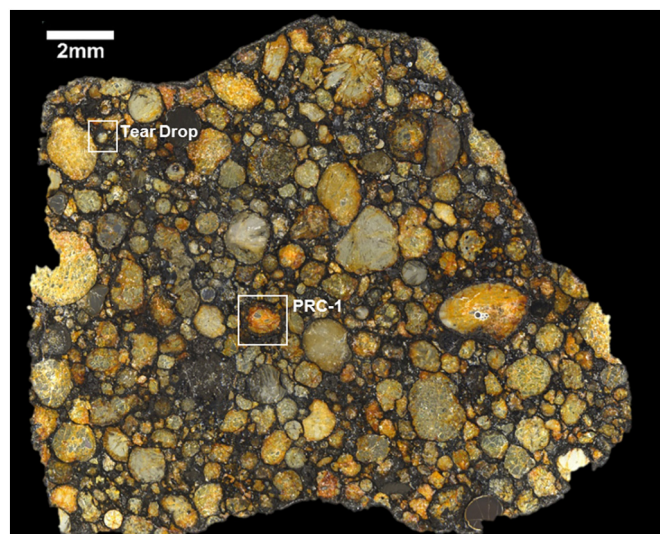


Fig. 1. Stereomicroscopic image of a polished thin section from the EET 14017. The white rectangles indicate studied chondrules: Tear Drop in Fig. 5 and plagioclase rich chondrule (PRC-1) in Figs. 6, 7, and 8.

(EDS) was performed at 10 keV for small regions < 2 μm to minimize volume where X-rays are generated. Natural and synthetic mineral standards from Smithsonian and JEOL including albite, MgO, SiO₂, Al₂O₃, microcline, wollastonite, fayalite, MnO, Cr₂O₃, and TiO₂ were used. Counting times on peak were 20 s. The mean atomic number (MAN) method and $\phi(\rho Z)$ method of Armstrong/Love Scott were used to correct background and matrix effects, respectively [39,40]. X-ray elemental maps of chondrules were obtained using the EPMA with a focused beam, a 100 nA beam current, dwell time of 10 ms per pixel, and with pixel size of 1.2 μm . A BSE image in Fig. 7B was obtained with a field emission scanning electron microscope (FE-SEM; JEOL JSM-7200F) at KOPRI using a 5 keV accelerating voltage, 4 nA beam current.

2.3. Raman Spectral Analysis

After observations and analyses with EPMA and SEM, we removed carbon film using a diamond suspension (0.2 μm particle size) on the sample because silicate mineral phases in the carbon-coated section are not distinguished with a reflected-light microscope of a Raman system. Raman experiments were performed at Thermo Fisher Scientific Korea using a DXR2xi system equipped with a diode-pumped, solid state laser and using 532 nm excitation. The power of the laser was tuned as 9.1 mW (on the sample surface, measured out of a $10\times$ objective). Acquisition consisted of ~ 0.2 s exposure time with 600 scans. The step size for both depth profiling and Raman line scan was 0.6 μm . The possible distance for depth profiling depends on a working distance of objective lens. The working distance of $100\times$ objective used in this study is 500 μm . The DXR2xi system was operated with the Thermo OMNIC acquisition software. Calibration of the spectrometer was checked on a silicon wafer before the analytical session.

The DXR2xi system used in this study is equipped with an electron multiplied charge-coupled device (EM CCD). The EM CCD amplifies transmitted Raman signals by producing electrons when laser photon impinges camera. It enables to get a large signal-to-noise ratio (S/N) in a short time. Therefore, it is possible to analyze samples that are easily damaged by laser, and to obtain high-resolution Raman imaging within a short time. Raman spectra of olivine in a chondrule of EET 14017 with and without EM CCD were obtained at the same site (Fig. 2). Note that the results did not show any change in Raman peak position. The S/N of Raman spectra was obtained by dividing the maximum intensity of signals by that of noise, the value was ~ 35 without EM CCD and ~ 51 with EM CCD. All data in this study were obtained with EM CCD.

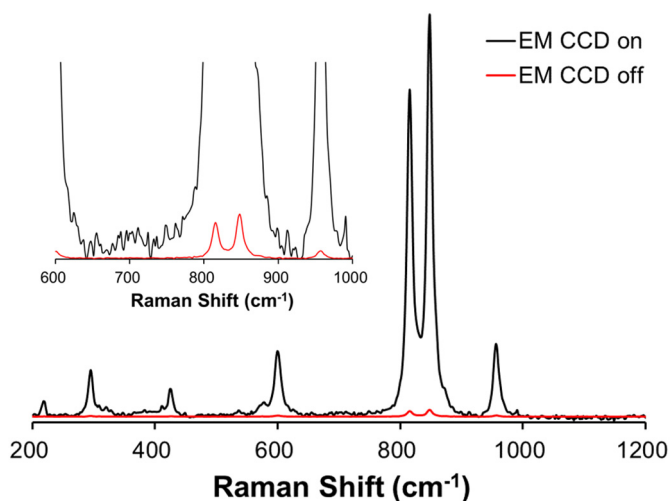


Fig. 2. Electron multiplied charge-coupled device (EM CCD) on/off comparison of Raman spectra of olivine in a chondrule of EET 14017 where 825 and 858 cm^{-1} bands are observed. The signal-to-noise ratio (S/N) is ~ 35 without EM CCD and ~ 51 with EM CCD.

3. Results and Discussion

Both lateral and depth resolutions in confocal Raman spectroscopy analysis are determined by magnification of objective lens and wavelength of laser [41]. The theoretical lateral resolution of DXR2xi system is $\sim 0.7 \mu\text{m}$ using a 532 nm laser and a 100 \times objective from the equation of $1.22\lambda/\text{NA}$ based on the Airy function, where λ is the wavelength of laser and NA (the numerical aperture of the objective lens) is 0.9 in this study. A line profile on a chondrule in the EET 14017 was obtained with a step size of $0.5 \mu\text{m}$ (Fig. 3A–C), smaller than the theoretical lateral resolution, to determine the experimental lateral resolution of the confocal Raman for silicate minerals in this study. Bright red color denotes olivine, dark red color for pyroxene, and sky blue color for plagioclase, respectively, in the combined X-ray elemental map of Mg $K\alpha$ (red), Ca $K\alpha$ (green), and Al $K\alpha$ (blue) (Fig. 3A–B). The white line on the Fig. 3B shows the positions of Raman measurements at the boundary between olivine and pyroxene. The series of Raman spectra are shown in Fig. 3C.

The olivine bands (825 and 858 cm^{-1}) [e.g., 15,42] and pyroxene main bands (665, 690, 1013, and 1031 cm^{-1}) [e.g., 8,43] are observed. The peak intensities of olivine bands decrease and those of pyroxene bands increase toward the grain boundary. Normalized intensities of olivine peaks (at 825 cm^{-1}) obtained near the grain boundary in the pyroxene region decrease to 0 (Fig. 3C). The lateral resolution defined by the distance between upper 84% and lower 16% of normalized intensities of olivine peaks (at 825 cm^{-1}) is $\sim 1.0 \mu\text{m}$ with the DXR2xi confocal Raman system, when 532 nm laser and 100 \times objective are used (Fig. 4). The 16–84% resolution is given by Gaussian criterion and comparable to $0.85 \times 0.85 \times (1.22\lambda/\text{NA}/2)$ [44,45]. Thus, the experimental lateral resolution of $\sim 1.0 \mu\text{m}$ in silicate minerals using the DXR2xi system is about ~ 3 times worse than the theoretical value.

The EET 14017 chondrite is classified as petrologic type 3 because chondrules are clearly defined and glassy mesostasis is observed in numerous chondrules. A typical chondrule with glassy mesostasis is shown in Fig. 5. Olivine (dark gray), pyroxene (gray), mesostasis (light gray), and metal (white) are observed in the BSE image of the “Tear Drop (TD)” chondrule (Fig. 5A). Site 1 and 2 are the analyzed positions to get Raman spectra and depth profile on the olivine and mesostasis regions, respectively. Although it is easy to distinguish olivine and pyroxene grains from mesostasis, it is difficult to probe whether the phase of mesostasis is amorphous or crystalline. Raman spectra of olivine and mesostasis obtained from sites 1 and 2 are presented in Fig. 5B. Raman spectrum of olivine shows peaks at 825 and 858 cm^{-1} that are main bands of olivine [15,42] and that of the mesostasis shows broad feature indicating it is amorphous [2,46]. Weak intensities of 825 and 858 cm^{-1} peaks are also observed in Raman spectrum of glassy mesostasis, probably originated from olivine underneath the surface. Two lines of evidences support it. It is well known that Raman intensity of a crystal is significantly stronger than that of glass. The theoretical depth resolution is defined by the equation of $2\lambda n/(\text{NA})^2$ [41], where λ is the wavelength of laser (532 nm), n is the refractive index of glass (~ 1.4) and NA is the numerical aperture of the objective lens (0.9). It is $\sim 2 \mu\text{m}$ and thus ~ 3 times poorer than the theoretical lateral resolution. However, the calculated depth resolution is given without considering the effect of refraction thus generally underestimated by a factor of ~ 2 [47,48].

Depth profiling was performed to confirm the presence of olivine under the glassy mesostasis and the result is shown in Fig. 5C. Raman

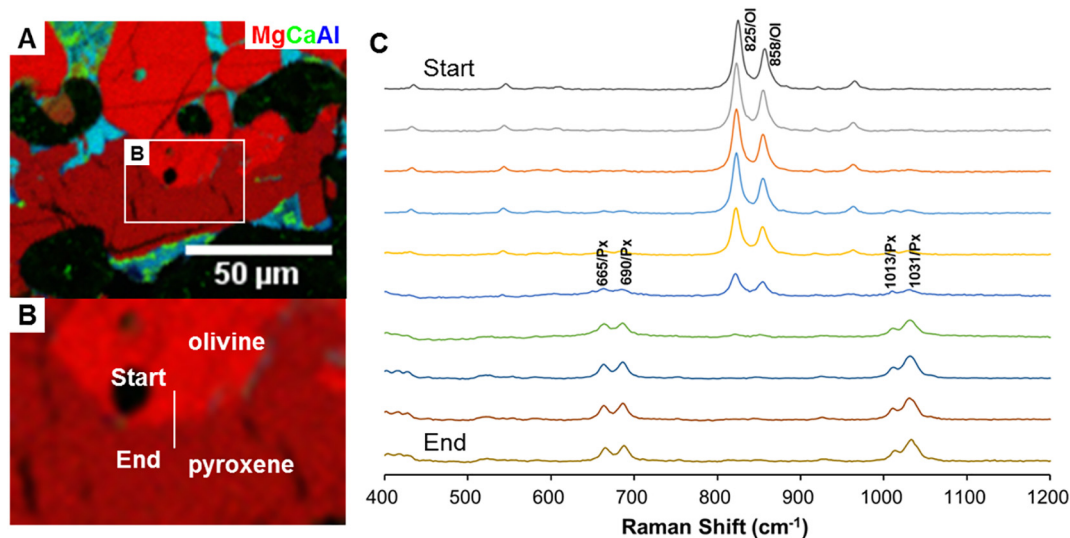


Fig. 3. (A) Combined X-ray elemental map in Mg $K\alpha$ (red), Ca $K\alpha$ (green), and Al $K\alpha$ (blue) of olivine and pyroxene in chondrule showing different locations with Raman measurements. Bright red color denotes olivine, dark red color for pyroxene, and sky blue color for plagioclase. (B) Magnification of the white rectangle in (A). The white line shows Raman measurements across the grain boundary between olivine and pyroxene. (C) Raman profile of 10 points from the white line in (B) are visible at right. Ol = olivine; Px = pyroxene. The peak intensities of olivine band (825 and 858 cm^{-1}) decrease and those of pyroxene band (665, 690, 1013, and 1031 cm^{-1}) increase across the boundaries of olivine and pyroxene.

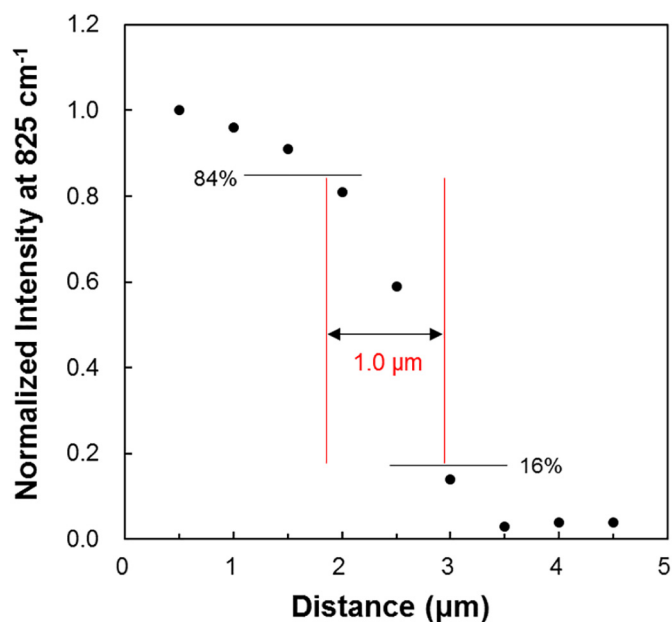


Fig. 4. Normalized Raman intensity at 825 cm^{-1} with varying distance from olivine grain. The experimental lateral resolution defined by width between 16% and 84% level is calculated to be $\sim 1.0\text{ }\mu\text{m}$.

intensity of the 825 cm^{-1} peak (one of the main bands of olivine) is presented in color with scale bar. Note that red area (Raman intensities around 6000 at the 825 cm^{-1} peak) represents olivine and blue area

(Raman intensities around 100) for glassy mesostasis. The color of Raman intensities on the surface at site 2 appears blue and that of the apparent depth of $5\text{ }\mu\text{m}$ appears red by increasing the peak intensity of olivine. The result indicates that glassy mesostasis is present on the surface and olivine exist below the surface. Considering that both the apparent thickness and depth below the surface are generally about half of the true values [47], we estimate the olivine is present at the depth of $\sim 10\text{ }\mu\text{m}$.

Through the observations done with optical microscope and the BSE images obtained with the EPMA and SEM, we found a plagioclase-rich chondrule (PRC-1) in the EET 14017, which contains two different occurrences of plagioclase: lath-shaped and interstitial plagioclase (Fig. 6). PRC-1 shows porphyritic texture with euhedral olivine grains, low-Ca and high-Ca pyroxene, and minor metal. Olivine is nearly forsterite ($\text{Fo}99.5 \pm 0.2$; 2σ) and contains $\sim 0.5\text{ wt\%}$ of CaO (Table 1). Low-Ca pyroxene is close to enstatite composition ($\text{Wo}0.9 \pm 0.2\text{En}97.9 \pm 0.4$) and high-Ca pyroxene has variable amount of CaO ($4.1\text{--}20.5\text{ wt\%}$) and minor TiO_2 and Al_2O_3 (Table 1). Lath-shaped plagioclase containing small amount of Na_2O ($\sim 0.7\text{ wt\%}$) generally occurs in the core (Fig. 6 and details in Fig. 7), whereas interstitial plagioclase having more Na_2O ($\sim 1.3\text{ wt\%}$) is present in the outside of the chondrule (Fig. 6 and details in Fig. 8).

Fig. 7A–B shows lath-shaped plagioclase together with high-Ca pyroxene, and mesostasis. Texturally the lath-shaped plagioclase crystallized from a melt, followed by high-Ca pyroxene. The detailed texture of the mesostasis is shown in the BSE image obtained with FE-SEM at 5 keV accelerating voltage (Fig. 7B). The mesostasis consists of two different phases (dark and light gray colors) of $100\text{--}200\text{ nm}$ in width, which are too small to be chemically identified with EDS or WDS.

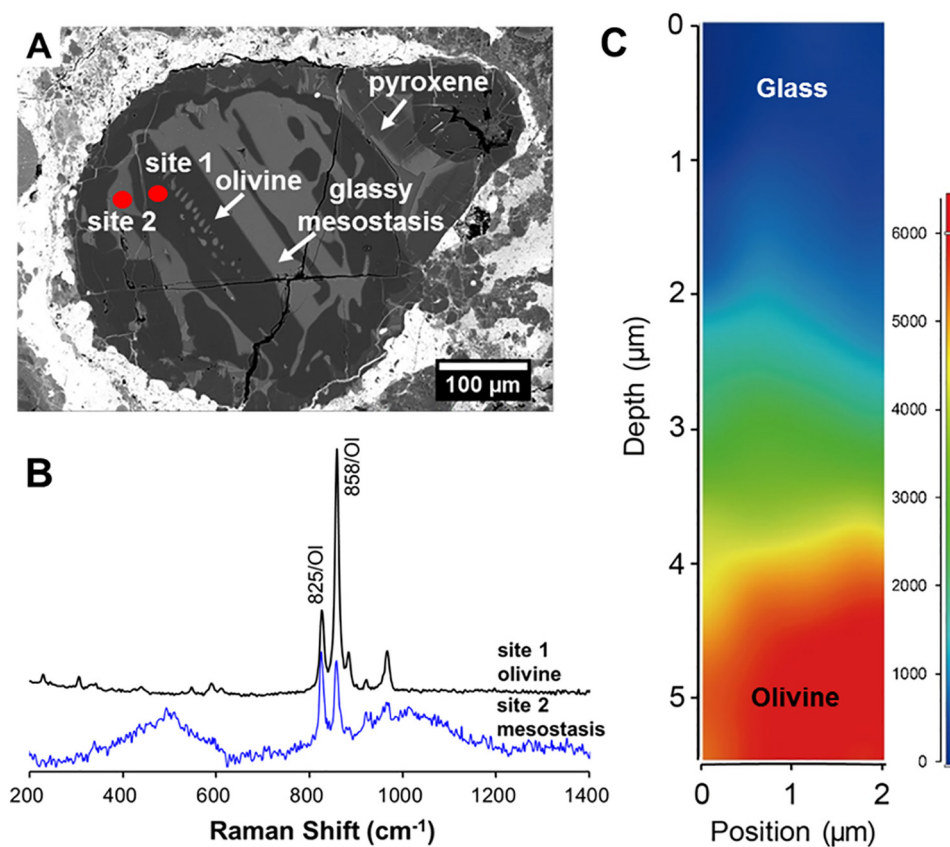


Fig. 5. (A) Backscattered electron (BSE) image of a “Tear Drop” chondrule with glassy mesostasis (light gray color) in EET 14017. Dark gray color denotes olivine, gray color for pyroxene. (B) Raman spectra of site 1 (black line) and 2 (blue line) in (A) showing main bands of olivine (825 and 858 cm^{-1}) and glass features, respectively. (C) Depth profiling of Raman band intensities of 825 cm^{-1} peak at site 2. A full Raman spectrum is acquired in every pixel, but only Raman intensities of 825 cm^{-1} peak are imaged to distinguish glass and olivine.

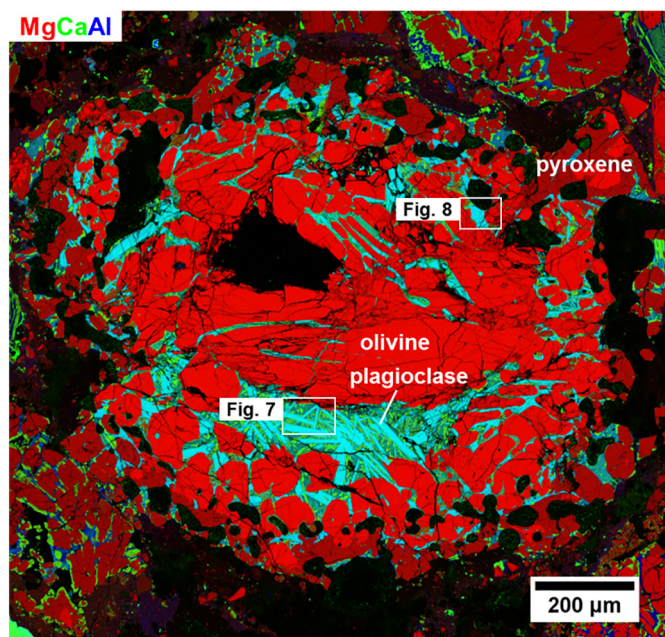


Fig. 6. Combined X-ray elemental map in Mg K α (red), Ca K α (green), and Al K α (blue) of plagioclase-rich chondrule (PRC-1) in EET 14017, which contains both lath-shaped and interstitial plagioclase. The white squares indicate the regions in Figs. 7 and 8.

To confirm whether the plagioclase grains in Fig. 7A are crystalline and to get structural information, it is necessary to use Raman spectroscopy. Raman spectra were acquired at site 3 on a lath-shaped plagioclase and site 4 on mesostasis region. Raman spectra on the surface and at a nominal depth of 5 μm at site 3 are shown in Fig. 7C. Main bands of plagioclase (488 and 505 cm^{-1}) [12,14] are observed on the

surface, indicating plagioclase grains are crystalline. A weak intensity of 461 cm^{-1} band is also observed on the surface of site 3. Since the experimental lateral resolution of the Raman spectroscopy in this study is $\sim 1.0 \mu\text{m}$ (Fig. 4) but the depth resolution is much poorer, the weak band of 461 cm^{-1} is likely caused by subsurface minerals. Raman spectrum of site 3 at a nominal depth of 5 μm clearly shows 461 cm^{-1} band as well as main bands of plagioclase (488 and 505 cm^{-1}) (Fig. 7C). Since the 461 cm^{-1} band is not consistent with main bands of olivine and pyroxene adjacent plagioclase, we obtained Raman spectra of a mesostasis region (site 4 in Fig. 7B) between plagioclase and high-Ca pyroxene, having 461, 508, 668, and 1013 cm^{-1} bands (Fig. 7D). Hence the 461 cm^{-1} peak in Fig. 7C could be originated from mesostasis which is expected to be present under the lath-shaped plagioclase. Despite that the width of the mesostasis is only $\sim 2 \mu\text{m}$ (Fig. 7B), Raman spectrum from the mesostasis unlikely contain peaks from adjacent minerals under confocal mode giving the experimental lateral resolution of $\sim 1.0 \mu\text{m}$.

As aforementioned, chondrules in primitive chondrites (type 3) generally retain glassy mesostasis resulted from rapid cooling rate (up to $\sim 2000 \text{ }^\circ\text{C/h}$) [26]. Most of mesostases in the chondrules of EET 14017 also remain as amorphous as seen in Fig. 5. However, Raman spectrum of the mesostasis in PRC-1 (Fig. 7D) shows several sharp peaks, indicating it is not an amorphous phase but consists of tiny minerals as seen in Fig. 7B. A quantitative analysis for individual phases of the mesostasis using WDS is difficult due to their small sizes (100–200 nm in width). Instead, qualitative chemical composition of the mesostasis region was acquired using EDS, consisted of $\sim 70 \text{ wt}\%$ SiO_2 , $\sim 17 \text{ wt}\%$ Al_2O_3 , $\sim 9 \text{ wt}\%$ CaO, $\sim 1 \text{ wt}\%$ MgO, $\sim 1 \text{ wt}\%$ FeO, $\sim 1 \text{ wt}\%$ Na_2O , and $<1 \text{ wt}\%$ TiO_2 . Based on the composition, silica and plagioclase will be most likely for the phases in the mesostasis. It is also supported by dark and light gray colors in the BSE image (Fig. 7B). Thus, the observed 461 and 508 cm^{-1} bands may be from submicrometer-sized quartz and plagioclase in the mesostasis, respectively. Previous studies for silica-rich chondrules and clasts suggested that they can be originated from silica-rich precursors, probably formed by fractional condensation in

Table 1
EPMA analyses of minerals in the plagioclase-rich chondrule (PRC-1) from the Elephant Moraine 14017.

	Olivine (n [†] = 20)		Low-Ca pyroxene (n = 10)		High-Ca pyroxene (n = 9)		Lath-shaped plagioclase (n = 10)		Interstitial plagioclase (n = 9)	
	Average	2 σ	Average	2 σ	Average	2 σ	Average	2 σ	Average	2 σ
SiO ₂	41.97	0.39	58.57	0.55	52.71	3.68	46.34	1.30	47.69	1.81
TiO ₂	0.08	0.06	0.15	0.08	1.28	1.10	0.02	0.04	0.03	0.04
Al ₂ O ₃	0.32	0.32	0.67	0.30	3.46	2.17	32.05	0.93	30.64	1.87
Cr ₂ O ₃	0.16	0.15	0.48	0.07	1.05	1.18	0.02	0.03	0.03	0.01
FeO	0.51	0.25	0.85	0.24	1.37	2.06	0.21	0.19	0.46	0.37
MnO	0.01	0.03	0.04	0.05	0.28	0.32	nd	nd	nd	nd
MgO	56.17	0.44	38.82	0.24	22.70	10.55	0.82	0.19	1.03	0.24
CaO	0.52	0.13	0.50	0.11	16.58	11.33	18.87	0.51	17.81	1.04
Na ₂ O	0.01	0.02	0.00	0.01	0.05	0.10	0.68	0.21	1.26	0.77
K ₂ O	nd [‡]		nd		0.00	0.02	nd		0.00	0.01
Total	99.74	0.60	100.08	0.70	99.50	0.71	99.01	0.65	98.96	0.70
	4 oxygen		6 oxygen				8 oxygen			
Si	0.990	0.007	1.971	0.013	1.885	0.068	2.160	0.048	2.220	0.078
Ti	0.001	0.001	0.004	0.002	0.034	0.030	0.001	0.001	0.001	0.001
Al	0.009	0.009	0.026	0.012	0.147	0.096	1.760	0.059	1.681	0.104
Cr	0.003	0.003	0.013	0.002	0.030	0.035	0.001	0.001	0.001	0.000
Fe	0.010	0.005	0.024	0.007	0.041	0.064	0.008	0.007	0.018	0.015
Mn	0.000	0.001	0.001	0.001	0.009	0.010	nd	nd	nd	nd
Mg	1.976	0.008	1.948	0.011	1.206	0.505	0.057	0.013	0.071	0.016
Ca	0.013	0.003	0.018	0.004	0.639	0.445	0.942	0.029	0.888	0.052
Na	0.000	0.001	0.000	0.001	0.004	0.007	0.061	0.019	0.114	0.070
K	nd		nd		0.000	0.001	nd		0.000	0.000
Total	3.003	0.003	4.005	0.007	3.994	0.019	4.990	0.013	4.995	0.036
Fo		99.5		0.2						
Wo				0.9		34.0		23.9		
An							93.9	1.9	88.6	6.8

n[†]: number of analyses. nd[‡]: not detected. Detection limit is 0.02 wt% (3 σ) for SiO₂, TiO₂, and Cr₂O₃, 0.03 wt% for FeO and MnO, 0.01 wt% for Al₂O₃, MgO, and Na₂O, and 0.005 wt% for CaO and K₂O.

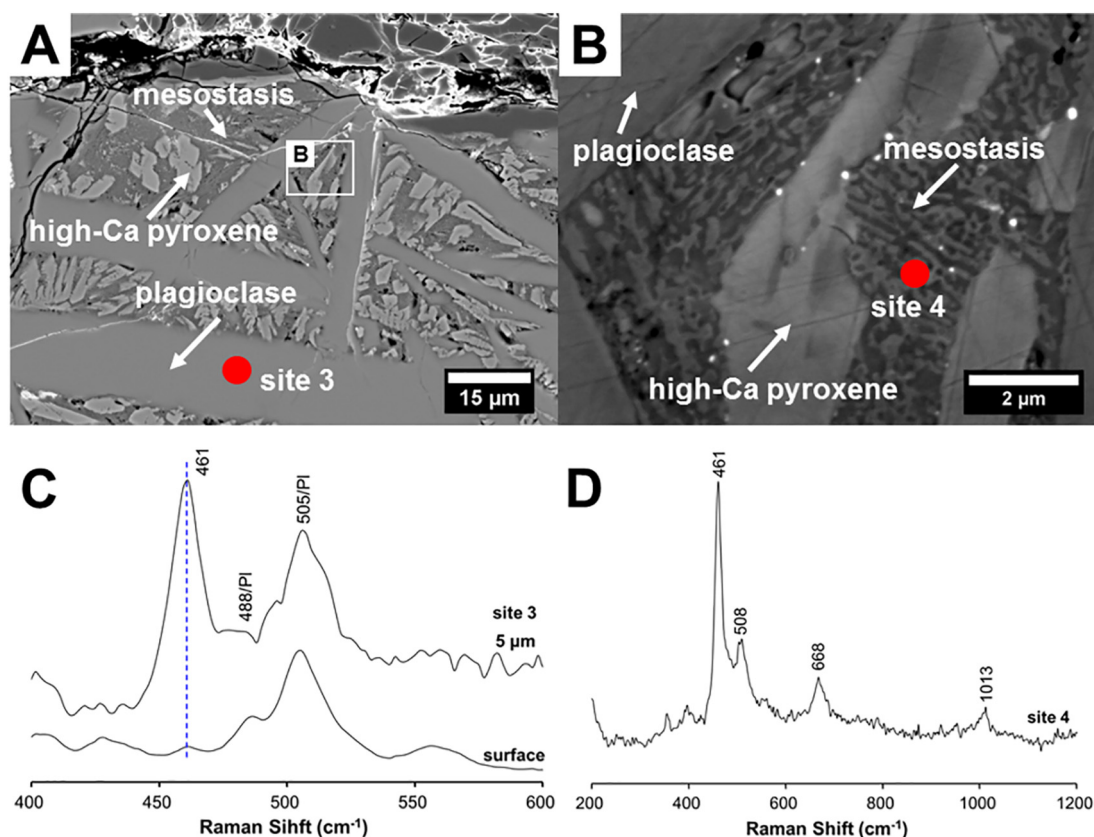


Fig. 7. (A) Backscattered electron (BSE) image of lath-shaped plagioclase (gray color) in plagioclase-rich chondrule (PRC-1) of EET 14017. Bright gray color denotes high-Ca pyroxene, dark gray color for mesostasis. (B) Magnification of the white rectangle in (A). (C) Raman spectra acquired on the surface and at a nominal depth of 5 μm of site 3. Main bands of plagioclase (488 and 505 cm^{-1}) are observed on the surface while 461 cm^{-1} band is also observed at 5 μm nominal depth. Pl = plagioclase. (D) Raman spectrum of mesostasis (site 4) in plagioclase-rich chondrule (PRC-1) showing 461, 508, 668, and 1013 cm^{-1} .

the solar nebula [13,49]. The bulk composition of PRC-1, however, is similar with that of a typical type I chondrule [50,51] and the mesostasis in chondrule of primitive chondrite has a similar composition to the EDS result of the mesostasis of PRC-1 [52]. Crystalline mesostasis composed of plagioclase and silica of PRC-1 is very similar to those of plagioclase-rich chondrules in the reduced CV chondrites [35]. A dynamic crystallization experiment showed that both the lath-shaped plagioclase and fine-grained plagioclase in the mesostasis can be formed at slow cooling rate (~ 10 $^{\circ}\text{C}/\text{h}$) but no silica phase was reproduced [33]. The presence of quartz in the mesostasis of PRC-1 may suggest that the chondrule cooled slower than typical type I chondrules. The weak intensities of 668 and 1013 cm^{-1} bands in the mesostasis are expected to be generated from subsurface pyroxene grains if considering the Mg-poor compositions of the mesostasis.

The 461 and 508 cm^{-1} bands are different from the characteristic bands of quartz (464 cm^{-1}) and anorthitic plagioclase (505 cm^{-1}), respectively. The observed peak shift of quartz and plagioclase may result from structural and/or compositional changes in those minerals [53,54]. The 464 cm^{-1} band of quartz at atmospheric pressure can shift toward the lower wavenumber due to tensile normal stress at the low pressure and temperature [53]. Thus the 461 cm^{-1} band observed in the mesostasis of PRC-1 chondrule may give an insight into the thermal and shock histories in the solar nebula. Raman peaks of plagioclase vary with structural and compositional change. The 508 cm^{-1} band observed in the mesostasis is a characteristic peak of albitic plagioclase [54], which is unlikely the Na-poor composition of the mesostasis. The Raman peak shift of plagioclase in the mesostasis might be due to poor crystallinity of tiny plagioclase grains.

An interstitial plagioclase grain (gray), olivine (dark gray), high-Ca pyroxene (light gray), and metal (white) are observed in PRC-1

(Fig. 8A). Site 5 is the analyzed region with 2 μm width and 10 μm depth for Raman spectroscopy. The largest plagioclase grain in the chondrule is ~ 20 μm wide. Fig. 8B shows Raman spectra of plagioclase obtained from the surface and a nominal depth of 5 μm at site 5 under confocal mode. Raman spectrum obtained from the surface has peaks at 488 and 505 cm^{-1} that are the main bands of plagioclase [14,55] and weak peaks at 700 and 980 cm^{-1} that are the main bands of pyroxene. Thus the interstitial plagioclase grain in Fig. 8A is crystalline and weak peaks at 700 and 980 cm^{-1} are likely from a subsurface pyroxene. Raman spectrum obtained from the nominal depth of 5 μm has strong 668, 682 and 1013 cm^{-1} bands of pyroxene but weak 488 and 505 cm^{-1} bands of plagioclase. Note that the peak intensity of pyroxene increases remarkably with increasing depth as in the depth profiling result (Fig. 8C) and that the true thickness of the plagioclase and positional depth of the pyroxene may become twice the nominal depth [47]. Raman intensities of the 1013 cm^{-1} peak (one of the main bands of pyroxene) are shown in color with scale bar. Note that the red color (Raman intensities around 2500 at the 1013 cm^{-1} peak) represents pyroxene while the blue color (Raman intensities of 100) represents plagioclase. By decreasing the peak intensity of pyroxene, the color changes from red to blue. Considering the effect of refraction [47], pyroxene is estimated to be present at ~ 10 μm depth under the plagioclase.

The co-occurrence of lath-shaped and interstitial plagioclase in the PRC-1 may constrain cooling history of the chondrule in the solar nebula. The crystallization sequence of the PRC-1 inferred from the texture is olivine, low-Ca pyroxene, followed by plagioclase, high-Ca pyroxene, and mesostasis. Lath-shaped plagioclase generally occurs together with high-Ca pyroxene and mesostasis, whereas interstitial plagioclase is present without mesostasis between olivine and pyroxene in the

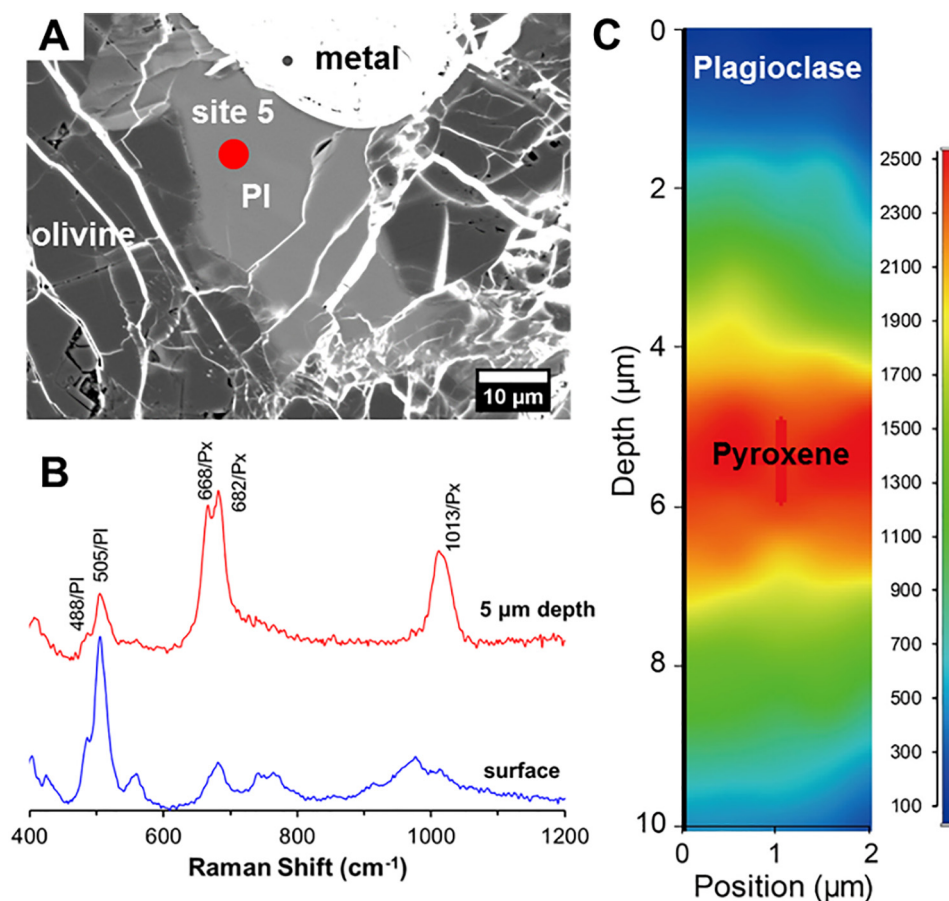


Fig. 8. (A) Backscattered electron (BSE) image of interstitial plagioclase in plagioclase-rich chondrule (PRC-1) of EET 14017. (B) Raman spectra of site 5 in (A) with varying depth. The blue line shows Raman spectrum collected from surface of site 5 and red line shows that from a nominal depth of 5 μm . (C) Composite image of Raman band intensities of site 5. A full Raman spectrum of each pixel is acquired, but only relative intensities of spectra for plagioclase (PI) and pyroxene (Px) are imaged.

PRC-1. Lath-shaped plagioclase contains less Na_2O (~ 0.7 wt% in average) compared to interstitial plagioclase (~ 1.3 wt%) (Table 1). The dynamic crystallization experiments from olivine-rich chondrule melts showed that lath-shaped plagioclase crystallized at faster cooling rates (>50 $^\circ\text{C}/\text{h}$) and interstitial plagioclase formed at slower cooling rates (<10 $^\circ\text{C}/\text{h}$) [33]. Both the less Na_2O content in the lath-shaped plagioclase and the co-occurrence of mesostasis are consistent with fast cooling rates. On the other hand, the more Na_2O content in the interstitial plagioclase and the absence of mesostasis agree with slow cooling rates. Although the lath-shaped and interstitial plagioclase grains in the PRC-1 have different shape, Na_2O content, mineral assemblage, and inferred cooling rate, Raman peaks from the both plagioclase are almost identical (Figs. 7C and 8B), implying that Raman spectroscopy has some specific limitation for providing constraints on the cooling history of chondrules in the solar nebula.

In spite of some limitation, Raman spectroscopy has advantages over other spectroscopic methods (e.g., nuclear magnetic resonance, X-ray scattering, and X-ray absorption spectroscopy) in the study of extraterrestrial materials. Raman spectroscopy is a non-destructive, in-situ, and fast analytical method without complex sample preparation and any significant damage on the sample. High-lateral resolution and well-resolved depth profiling with the confocal Raman spectroscopy enable us to reveal submicrometer-sized phases and to investigate hidden phases underneath the surface without destruction of the sample. Especially a combined study of Raman spectroscopy together with electron microprobe is powerful for the thorough study to

understand the structure and chemistry of mineral components of extraterrestrial materials.

4. Conclusion

The experimental data presented here provide identification of chondrule minerals and subsurface mineral phases through depth profiling in a primitive chondrite. An experimental lateral resolution of the Thermo Fisher Scientific DXR2xi system for silicate minerals is ~ 1.0 μm when a $100\times$ objective and a 532 nm laser are used. Raman spectrum of mesostasis in the TD chondrule of EET 14017 confirms that the mesostasis remains amorphous and depth profiling results demonstrate the presence of olivine under the glassy mesostasis in that chondrule. Raman spectra on a lath-shaped plagioclase in PRC-1 show main bands of plagioclase (488 and 505 cm^{-1}) and weak intensity of 461 cm^{-1} band. Raman spectrum from the mesostasis adjacent to the lath-shaped plagioclase shows sharp 461 and 508 cm^{-1} bands, suggestive of submicrometer-sized quartz and plagioclase in the mesostasis. The weak 461 cm^{-1} peak from the lath-shaped plagioclase is probably from the subsurface quartz in the mesostasis. The mesostasis composed of crystalline plagioclase and quartz in PRC-1 may imply that the chondrule cooled slower than typical type I chondrules. Raman spectrum of interstitial plagioclase in PRC-1 shows 488 and 505 cm^{-1} bands and weak pyroxene bands. Depth profiling conducted on the plagioclase clearly shows that pyroxene exists below the surface. Confocal Raman spectroscopy can non-destructively probe submicrometer-sized phases and subsurface minerals in a

short time without complex sample preparation, which could be powerful to study extraterrestrial materials.

Acknowledgement

We thank Mrs. Minjung Son at Thermo Fisher Scientific Korea for her assistance in using the DXR2xi Raman microscope. This work was supported by Korea Polar Research Institute project PM18030 (20140409). Two anonymous reviewers for their comments and Dr. Malgorzata Baranska for editorial handling are kindly acknowledged.

References

- [1] C.V. Raman, K.S. Krishnan, A new type of secondary radiation, *Nature* 121 (1928) 501.
- [2] D.R. Neuville, D.D. Ligny, G.S. Henderson, *Advances in Raman spectroscopy: applied to earth and material sciences, Reviews in Mineralogy and Geochemistry* 2014, pp. 509–541.
- [3] A. Wang, B.L. Jolliff, L.A. Haskin, Raman spectroscopic characterization of a Martian SNC meteorite: Zagami, *J. Geophys. Res.-Planet* 104 (1999) 8509–8519.
- [4] T.F. Cooney, E.R. Scott, A.N. Krot, S.K. Sharma, A. Yamaguchi, Vibrational spectroscopic study of minerals in the Martian meteorite ALH84001, *Am. Mineral.* 84 (1999) 1569–1576.
- [5] O. Unsalan, A. Yilmaz, O. Bolukbasi, B. Ozturk, H.H. Esenoglu, G.O. Ildiz, C.Y. Ornek, Micro-Raman, FTIR, SEM-EDX and structural analysis of the Çanakkale meteorite, *Spectrochim. Acta A* 92 (2012) 250–255.
- [6] H.G.M. Edwards, D.W. Farwell, M.M. Grady, D.D. Wynn-Williams, I.P. Wright, Comparative Raman microscopy of a Martian meteorite and Antarctic lithic analogues, *Planet. Space Sci.* 47 (1999) 353–362.
- [7] A.G. Dall'Asén, S.I. Dimas, S. Tyler, J.F. Johnston, T.R. Anderton, I.I. Ivans, J.M. Gerton, B.C. Bromley, S.J. Kenyon, Mapping the composition of chondritic meteorite Northwest Africa 3118 with micro-Raman spectroscopy, *Spectrosc. Lett.* 50 (2017) 417–425.
- [8] Z. Bidong, S.R. Shieh, A.C. Withers, A. Bouvier, Raman spectroscopy of shocked enstatite-rich meteorites, *Meteorit. Planet. Sci.* (2018), <https://doi.org/10.1111/maps.13106>.
- [9] L. Pittarello, K. Baert, V. Debaille, P. Claeys, Screening and classification of ordinary chondrites by Raman spectroscopy, *Meteorit. Planet. Sci.* 50 (2015) 1718–1732.
- [10] L. Bonal, E. Quirico, M. Bourot-Denise, G. Montagnac, Determination of the petrologic type of CV3 chondrites by Raman spectroscopy of included organic matter, *Geochim. Cosmochim. Acta* 70 (2006) 1849–1863.
- [11] A. Kereszturi, I. Gyollai, Z. Kereszty, K. Kiss, M. Szabo, Z. Szalai, M. Ringer, M. Veres, Analyzing Raman - infrared spectral correlation in the recently found meteorite Csatalja, *Spectrochim. Acta A Mol. Biomol. Spectrosc.* 173 (2017) 637–646.
- [12] S. Nagy, S. Józsa, A. Gucsik, S. Bérczi, K. Ninagawa, H. Nishido, M. Veres, Á. Kereszturi, H. Hargitai, Shock and thermal annealing history of the ALH 77005 Martian meteorite: a micro-Raman spectroscopic investigation, *Cent. Eur. Geol.* 55 (2012) 33–48.
- [13] D.C. Hezel, H. Palme, L. Nasdala, F.E. Brenker, Origin of SiO₂-rich components in ordinary chondrites, *Geochim. Cosmochim. Acta* 70 (2006) 1548–1564.
- [14] R. Le Parc, B. Champagnon, J. Dianoux, P. Jarry, V. Martinez, Anorthite and CaAl₂Si₂O₈ glass: low frequency Raman spectroscopy and neutron scattering, *J. Non-Cryst. Solids* 323 (2003) 155–161.
- [15] K.E. Kuebler, B.L. Jolliff, A. Wang, L.A. Haskin, Extracting olivine (Fo-Fa) compositions from Raman spectral peak positions, *Geochim. Cosmochim. Acta* 70 (2006) 6201–6222.
- [16] A. Kereszturi, I. Gyollai, M. Szabó, Case study of chondrule alteration with IR spectroscopy in NWA 2086 CV3 meteorite, *Planet. Space Sci.* 106 (2015) 122–131.
- [17] M.L. Frezzotti, F. Tecce, A. Casagli, Raman spectroscopy for fluid inclusion analysis, *J. Geochem. Explor.* 112 (2012) 1–20.
- [18] T. Tobała, Raman spectroscopy of organic, solid and fluid inclusions in the Oldest Halite of LGOM area (SW Poland), *Spectrochim. Acta A* 189 (2018) 381–392.
- [19] T. Kawamoto, A. Hertwig, H.-P. Schertl, W.V. Maresch, Fluid inclusions in jadeite and jadeite-rich rock from serpentinite mélanges in northern Hispaniola: trapped ambient fluids in a cold subduction channel, *Lithos* 308–309 (2018) 227–241.
- [20] M.K. Weisberg, M. Kimura, Petrology and Raman spectroscopy of high pressure phases in the Gujba CB chondrite and the shock history of the CB parent body, *Meteorit. Planet. Sci.* 45 (2010) 873–884.
- [21] A. Kereszturi, K. Fintor, I. Gyollai, Z. Kereszty, M. Szabo, Z. Szalai, H. Walter, Shock heterogeneity and shock history of the recently found ordinary Csatalja chondrite in Hungary, 2018, *Geol. Quart.* 62 (2018) 433–446.
- [22] K. Fintor, C. Park, S. Nagy, E. Pál-Molnár, A.N. Krot, Hydrothermal origin of hexagonal CaAl₂Si₂O₈ (dmisteinbergite) in a compact type A CAI from the Northwest Africa 2086 CV3 chondrite, *Meteorit. Planet. Sci.* 49 (2014) 812–823.
- [23] E.R.D. Scott, A.N. Krot, D.A. M., Chondrites and their components, *Meteorites, Comets, and Planets*, Elsevier 2013, pp. 66–137.
- [24] A.J. Brearley, A.N. Krot, *Metasomatism in the early solar system: the record from chondritic meteorites*, in: D.E. Harlov, H. Austrheim (Eds.), *Metasomatism and the Chemical Transformation of Rock: The Role of Fluids in Terrestrial and Extraterrestrial Processes*, Springer Berlin Heidelberg, Berlin, Heidelberg 2013, pp. 659–789.
- [25] G.R. Huss, A.E. Rubin, J.N. Grossman, Thermal metamorphism in chondrites, in: L.D. S, M.H. Y (Eds.), *Meteorites and the Early Solar System II*, University of Arizona Press 2006, pp. 567–586.
- [26] A.N. Krot, K. Keil, C.A. Goodrich, E.R.D. Scott, M. Weisberg, *Classification of Meteorites and their Genetic Relationships*, Elsevier, Oxford, 2014.
- [27] L. Bonal, E. Quirico, L. Flandinet, G. Montagnac, Thermal history of type 3 chondrites from the Antarctic meteorite collection determined by Raman spectroscopy of their polyaromatic carbonaceous matter, *Geochim. Cosmochim. Acta* 189 (2016) 312–337.
- [28] E. Quirico, P.-I. Raynal, M. Bourot-Denise, Metamorphic grade of organic matter in six unequilibrated ordinary chondrites, *Meteorit. Planet. Sci.* 38 (2003) 795–811.
- [29] A.E. Rubin, C. Ma, Meteoritic minerals and their origins, *Chem. Erde* 77 (2017) 325–385.
- [30] G.J. MacPherson, G.R. Huss, Petrogenesis of Al-rich chondrules: evidence from bulk compositions and phase equilibria, *Geochim. Cosmochim. Acta* 69 (2005) 3099–3127.
- [31] A. Bischoff, K. Keil, Ca–Al-rich chondrules and inclusions in ordinary chondrites, *Nature* 303 (1983) 588.
- [32] A. Bischoff, K. Keil, Al-rich objects in ordinary chondrites: related origin of carbonaceous and ordinary chondrites and their constituents, *Geochim. Cosmochim. Acta* 48 (1984) 693–709.
- [33] E.J. Tronche, R.H. Hewins, G.J. MacPherson, Formation conditions of aluminum-rich chondrules, *Geochim. Cosmochim. Acta* 71 (2007) 3361–3381.
- [34] Y.J. Sheng, I.D. Hutcheon, G.J. Wasserburg, Origin of plagioclase-olivine inclusions in carbonaceous chondrites, *Geochim. Cosmochim. Acta* 55 (1991) 581–599.
- [35] A.N. Krot, I.D. Hutcheon, K. Keil, Plagioclase-rich chondrules in the reduced CV chondrites: evidence for complex formation history and genetic links between calcium-aluminum-rich inclusions and ferromagnesian chondrules, *Meteorit. Planet. Sci.* 37 (2002) 155–182.
- [36] A.N. Krot, G.J. Macpherson, A.A. Ulyanov, M.I. Petaev, Fine-grained, spinel-rich inclusions from the reduced CV chondrites Efremovka and Leoville: I. Mineralogy, petrology, and bulk chemistry, *Meteorit. Planet. Sci.* 39 (2004) 1517–1553.
- [37] A.N. Krot, K.D. Mckeegan, S.S. Russell, A. Meibom, M.K. Weisberg, J. Zipfel, T.V. Krot, T.J. Fagan, K. Klaus, Refractory calcium-aluminum-rich inclusions and aluminum-diopside-rich chondrules in the metal-rich chondrites Hammadah al Hamra 237 and Queen Alexandra Range 94411, *Meteorit. Planet. Sci.* 36 (2001) 1189–1216.
- [38] M.J. Wick, R.H. Jones, Formation conditions of plagioclase-bearing type I chondrules in CO chondrites: a study of natural samples and experimental analogs, *Geochim. Cosmochim. Acta* 98 (2012) 140–159.
- [39] J.J. Donovan, T.N. Tingle, An improved mean atomic number background correction for quantitative microanalysis, *Microsc. Microanal.* 2 (1996) 1–7.
- [40] J.T. Armstrong, Quantitative analysis of silicate and oxide materials: comparison of Monte Carlo, ZAF and $\phi(\rho z)$ procedures, in: D.E. Newbury (Ed.), *Microbeam Analysis*, San Francisco Press, San Francisco, CA 1988, pp. 239–246.
- [41] T. Wilson, Confocal microscopy, in: T. Wilson (Ed.), *Confocal microscopy*, Academic Press, London 1990, pp. 1–64.
- [42] P. McMillan, Vibrational spectroscopy in the mineral sciences, in: S.W. Kieffer, A. Navrotsky (Eds.), *Microscopic to Macroscopic*, Mineralogical Society of America, Washington 1985, pp. 9–63.
- [43] E. Huang, C.H. Chen, T. Huang, E.H. Lin, J.-A. Xu, Raman spectroscopic characteristics of Mg-Fe-Ca pyroxenes, *Am. Mineral.* 85 (2000) 473.
- [44] B. Zhang, J. Zerubia, J.C. Olivo-Marin, Gaussian approximations of fluorescence microscope point-spread function models, *Appl. Opt.* 46 (2007) 1819–1829.
- [45] M.P. Seah, Resolution parameters for model functions used in surface analysis, *Surf. Interface Anal.* 33 (2002) 950–953.
- [46] B.O. Mysen, P. Richet, *Silicate Glasses and Melts: Properties and Structure*, Elsevier, Amsterdam, 2005.
- [47] N.J. Everall, Confocal Raman microscopy: why the depth resolution and spatial accuracy can be much worse than you think, *Appl. Spectrosc.* 54 (2000) 1515–1520.
- [48] T. Dieing, Resolution and performance of 3D confocal Raman imaging systems, in: J. Toporski, T. Dieing, O. Hollricher (Eds.), *Confocal Raman Microscopy*, Springer International Publishing, Cham 2018, pp. 121–153.
- [49] C.A. Brigham, H. Yabuki, Z. Ouyang, M.T. Murrell, A. El Goresy, D.S. Burnett, Silica-bearing chondrules and clasts in ordinary chondrites, *Geochim. Cosmochim. Acta* 50 (1986) 1655–1666.
- [50] R.H. Jones, Petrology of FeO-poor, porphyritic pyroxene chondrules in the Semarkona chondrite, *Geochim. Cosmochim. Acta* 58 (1994) 5325–5340.
- [51] R.H. Jones, E.R.D. Scott, Petrology and thermal history of type IA chondrules in the Semarkona (LL3.0) chondrite, *Proc. 19th Lunar Planet. Sci. Conf* 1989, pp. 523–536.
- [52] J.N. Grossman, A.J. Brearley, The onset of metamorphism in ordinary and carbonaceous chondrites, *Meteorit. Planet. Sci.* 40 (2005) 87–122.
- [53] Y. Kouketsu, T. Nishiyama, T. Ikeda, M. Enami, Evaluation of residual pressure in an inclusion-host system using negative frequency shift of quartz Raman spectra, *Am. Mineral.* 99 (2014) 433–442.
- [54] J.J. Freeman, A. Wang, K.E. Kuebler, B.L. Jolliff, L.A. Haskin, Characterization of natural feldspars by Raman spectroscopy for future planetary exploration, *Can. Mineral.* 46 (2008) 1477–1500.
- [55] T.P. Mernagh, Use of the laser Raman microprobe for discrimination amongst feldspar minerals, *J. Raman Spectrosc.* 22 (1991) 453–457.